J Mater Sci (2012) 47:5393–5401
DOI 10.1007/s10853-012-6422-2

Perovskite $La_{1-x}Sr_xGa_{1-y}Mn_yO_3$ solid solution crystals: Raman spectroscopy characterization

T. Runka · M. Berkowski

Received: 22 December 2011 / Accepted: 17 March 2012 / Published online: 10 April 2012

Abstract The first-order orthorhombic–rhombohedral phase transition of $La_{1-x}Sr_xGa_{1-y}Mn_yO_3$ (LSGMn) crystals is studied by Raman spectroscopy. An increase in Mn content causes significant changes in Raman spectra, especially in the high-wavenumber spectral range. The Raman spectrum of $La_{1-x}Sr_xGa_{1-y}Mn_yO_3$ compound with $x = y = 0.02$ is dominated by MnO_6 internal vibrations. Moreover, a change in the spectrum of this crystal is observed when the 785-nm excitation line is used. Essential reduction in the number of Raman modes during the phase transition is experimentally observed. The temperature of the phase transition decreases with increasing Sr and Mn contents, at the rate of about 20 K/at%.

Introduction

Lanthanum gallate-based family of perovskite crystals ($LaGaO_3$-based) are an important class of materials for applications as a substrates for ferroelectric thin films (e.g. $PbTiO_3$), high-T_c superconducting films (e.g. $YBa_2Cu_3O_7$) and colossal magnetoresistive film epitaxy [1, 2]. Moreover, lanthanum gallate doped with Sr and Mg (LSGM) at A- and B-sites, respectively, has been widely investigated as electrolyte material for IT-SOFCs because of its high-oxide ion conductivity [3–7]. The symmetry of the crystal structure is strongly dependent on the concentration of dopants (Sr and Mg). It has been reported that crystals with higher symmetry have better oxide ion conductivity [8, 9]. In recent years, lanthanum gallate compounds doped with Sr and Mn (LSGMn) or other transition metal elements have been extensively studied as good candidates for anode materials in LSGM-based SOFCs [10]. LSGMn compounds with high-Sr and -Mn doping level are promising anode materials thanks to their chemical and physical compatibility with electrolytes minimizing interfacial reactions, and they have thermal expansion coefficients similar to that of LSGM electrolyte. $LaGaO_3$ doped with Sr and Mn is also an interesting material because of the existence of first-order orthorhombic–rhombohedral (OR–RH) phase transition.

Lanthanum gallate crystals belong to ABO_3 oxide perovskite family. The larger rare earth La ions occupy the 12 coordinated A-sites and the smaller Ga ions occupy the octahedral B-sites in perovskite unit cell. At room temperature (RT), $LaGaO_3$ crystal has the centrosymmetric, OR structure of *Pbnm* (D_{2h}^{16}) symmetry. The *Pbnm* structure results from two equivalent anti-phase tilts around the x and y cubic axes and an in phase tilt around z axis ($b^-b^-c^+$ in Glazer notation), together with the displacement of cation A along the x, y OR directions. The high-temperature RH phase of $LaGaO_3$, in contrast, arises from equal anti-phase rotations around all three cubic axes ($a^-a^-a^-$). No shifts of A and B cations occur in this case. The $LaGaO_3$ crystal undergoes a structural phase transition at about 150 °C from OR *Pbnm* to non-centrosymmetric high-temperature phase of RH $R\bar{3}c$ symmetry [5, 11]. Recently, Glowacki et al. [3] reported RT X-ray investigation of $La_{1-x}Sr_xGa_{1-y}Mn_yO_3$ crystals. They have found that the structure of these crystals is described by OR *Pbnm* symmetry for $x = y = 0$, 0.02, 0.05 and $x = 0.05$, $y = 0.06$ compositions. Increase of Sr and Mn doping level

T. Runka (✉)
Faculty of Technical Physics, Poznan University of Technology,
ul. Nieszawska 13A, 60-965 Poznan, Poland
e-mail: tomasz.runka@put.poznan.pl

M. Berkowski
Institute of Physics, Polish Academy of Sciences,
Al. Lotników 32/46, 02-668 Warszawa, Poland

strongly decreases the OR–RH phase transition temperature of $La_{1-x}Sr_xGa_{1-y}Mn_yO_3$ crystals.

In this article, we report about structural changes related to a phase transition in the $LaGaO_3$ single crystals with lower Sr and Mn contents examined by Raman spectroscopy as a sensitive tool to monitor the crystallographic changes and structural distortions. It is expected that this method will provide both long-range and short-range structural information. One of the aims of this article is the determination of the doping level influence on phase transition temperature and vibrational properties of the crystals investigated.

Experimental

Single crystals of $LaGaO_3$ doped with Sr and Mn (LSGMn) were grown by the Czochralski method from the melt of the composition: $La_{1-x}Sr_xGa_{1-y}Mn_yO_3$ where $x = y =$ 0.005, 0.01 and 0.02. Starting materials (La_2O_3, Ga_2O_3) were heated at 1,000 °C and ($SrCO_3$, MnO_2) at 300 °C for 6 h before mixing in stoichiometric ratios and melting in a 40-mm iridium crucible. Single crystals with 20 mm diameter with convex crystal-melt interface were grown on (100) $LaGaO_3$-oriented seed at the pulling rate of 2 mm/h and a rotation of 20 rpm. The crystals were grown under ambient pressure in a nitrogen atmosphere containing 1 vol% of oxygen, they were red/light brown for a low-Sr and -Mn doping level ($x = y = 0.005$, 0.01), dark for $x = 0.02$ and dark/black for a higher doping level ($x = y > 0.05$) and have tendency to spiral growth. The tendency to spiral growth was decreased with increasing Mn content ($x = 0.05$, $y = 0.06$) [3].

The oriented samples A, B and C of $La_{1-x}Sr_xGa_{1-y}Mn_yO_3$ crystals with Sr and Mn content $x = y = 0.005$, 0.01 and 0.02, respectively, were prepared for Raman experiment. The samples of the size $2 \times 2 \times 2$ mm^3 were cut with the edges parallel to the axes of the laboratory co-ordinate system *XYZ*, where *X*||*a*, *Y*||*b* and *Z*||*c* (*a*, *b* and *c* are crystallographic axes of OR *Pbnm* structure of $La_{1-x}Sr_xGa_{1-y}Mn_yO_3$ crystals at RT).

Raman investigation of the oriented samples was carried out in the back-scattering geometry using a Renishaw inVia Raman microscope equipped with a confocal DM 2500 Leica optical microscope, a thermoelectrically (TE)-cooled CCD detector and two lasers: Ar^+ ion laser working at 488 and 514.5 nm, and an NIR laser working at 785 nm wavelength. The polarized Raman spectra were measured in the 70–900 cm^{-1} spectral range in a single scan with the exposure time of CCD detector in the range 120–200 s. The applied power of the laser beam before focusing with LWD 50× objective was kept in the range 0.2–0.5 mW, in order to avoid heating the sample locally by the laser beam. Edge filters were used to stray Rayleigh light rejection—the filters cut-off was 100 cm^{-1}. Complementary measurements in the low-wavenumber range (below 100 cm^{-1}) were carried out using a NExT filter (special device composed of double monochromator working in Czerny-Turner configuration being standard equipment of our Renishaw inVia Raman microscope). In both the cases, the instrumental resolution was better than 2 cm^{-1}. The position of Raman peaks was calibrated before collecting the data using a Si sample as an internal standard. The temperature measurements were performed using Linkam THMS 600 cooling/heating stage in the appropriate temperature range with a 0.1-K temperature step. The spectral parameters of Raman bands, such as the wavenumber of the peak centre position, intensity, integral intensity, and FWHM (full width at half maximum), were determined using the fitting procedure. All Raman bands were fitted with a Lorentzian line shape function. In order to obtain correct intensity of the first-order stokes Raman bands in temperature measurements, all spectra were fitted with the spectral response function: $S(v) = S_0(v)[1 + n(v)]$, where $n(v) = 1/(e^{hv/kT} - 1)$ is the Bose–Einstein population factor.

Spatially guided analysis of crystals surface was obtained from the spectra recorded in the point-by-point Raman mapping with 1.5 μm spacing between the points. Spatial resolution of the optical system during the collection of Raman maps is on comparable level for ×50 LWD objective (NA = 0.50—long working distance objective, $\lambda = 488$ nm).

Results and discussion

The group theory calculations performed for the OR *Pbnm* structure of the low-temperature phase of $La_{1-x}Sr_xGa_{1-y}Mn_yO_3$ crystals (primitive cell contains four chemical units—$Z_p = 4$) predicted the activity of the following modes:

$$\Gamma = 7A_g(\mathrm{R}) + 7B_{1g}(\mathrm{R}) + 5B_{2g}(\mathrm{R}) + 5B_{3g}(\mathrm{R}) + 8A_u(s) + 7B_{1u}(\mathrm{IR}) + 9B_{2u}(\mathrm{IR}) + 9B_{3u}(\mathrm{IR})$$

$$\Gamma_{ac} = B_{1u} + B_{2u} + B_{3u},$$

where R is the Raman-active modes, IR the infrared active modes, ac the acoustic modes and s is the silent modes.

Among all 60 normal modes predicted by the theory, only 24 are Raman active ($7A_g + 7B_{1g} + 5B_{2g} + 5B_{3g}$) [11–13]. These modes can be classified into two symmetric and four antisymmetric stretching modes, four bending modes and six rotation and tilt modes of the octahedra. At last eight modes are connected with the motion of A-site cations. All these modes are activated by four basic distortions of the ideal perovskite structure, i.e. rotations of

BO_6 octahedra around the cubic $[001]_c$ and $[110]_c$ axes, Jahn–Teller distortion, and La/Sr shift from its position in the ideal perovskite lattice. Analysis of literature data [14–16] implies that Raman spectra of $La_{1-x}Sr_xGa_{1-y}Mn_yO_3$ crystals of *Pbnm* structure will be dominated by the modes activated by $[110]_c$ rotation and Jahn–Teller distortions.

The high-temperature phase of $La_{1-x}Sr_xGa_{1-y}Mn_yO_3$ crystals has RH symmetry. The primitive unit cell contains two structural units ($Z_p = 2$), giving a total of 30 zone-centre phonons. The site symmetry group analysis performed for $R\bar{3}c$ space group leads to the following irreducible representation:

$$\Gamma = A_{1g} + 3A_{2g} + 2A_{1u} + 4A_{2u} + 4E_g + 6E_u$$

Among them, $A_{1g} + 4E_g$ are Raman-active modes, $3A_{2u} + 5E_u$ are IR active and the remaining $2A_{1u} + 3A_{2g}$ are silent modes. Raman-active modes can be classified into $A_{1g} + E_g$ rotational or tilt modes, E_g bending and E_g antistretching of BO_6 octahedra, and the remaining E_g is related to A-site cation movements. It is worth noticing that A_{2g} symmetric stretching mode is not allowed in the Raman spectrum. All these modes arise from *R*-point zone-boundary modes of the ideal perovskite structure of $Pm\bar{3}m$ symmetry.

Because the Raman spectra of the compounds investigated (samples A, B and C) show much similarities, we present in Fig. 1 the RT polarized spectra of a compound of the composition $La_{0.995}Sr_{0.005}Ga_{0.995}Mn_{0.005}O_3$ (sample A). The scattering configurations applied allow measurements of the Raman spectra with A_g (XX, YY, ZZ, X′Y′), B_{1g} (XY), B_{2g} (XZ), B_{3g} (ZY), $A_g + B_{1g}$ (X′X′, Y′Y′) symmetry. For better presentation, the spectra were arbitrarily shifted in the vertical direction.

A comparison of the Raman spectra of $La_{1-x}Sr_xGa_{1-y}Mn_yO_3$ crystals (see Fig. 2a) with those reported for $LaGaO_3$ crystal [5, 11] reveals essential differences in the spectral range above 480 cm^{-1}. There are no Raman modes in this range for $LaGaO_3$ crystal. However, depending on the composition of $La_{1-x}Sr_xGa_{1-y}Mn_yO_3$ crystals, some Raman modes are detected above 480 cm^{-1}. For lower Sr and Mn contents (samples A and B), a low-intense and broad band at about 675 cm^{-1} is observed, this mode but of a significantly higher intensity is also observed for sample C, and two additional broad bands are recorded at about 510 and 545 cm^{-1} (very low-intensity trace of these modes is observed for samples A and B as well). The appearance of these modes is certainly related to Mn atoms which occupy B-site octahedral positions, and they are assigned to internal vibrations of MnO_6 octahedra.

Analysis of the Raman spectra of reported OR compounds containing Mn atoms has shown that their spectra are basically dominated by MnO_6 octahedral vibrational modes. However, the RT investigation of $La_{1-x}Ca_xMnO_3$ compounds reported in [12, 16, 17] shows significant changes in Raman spectra with increasing Ca content. The

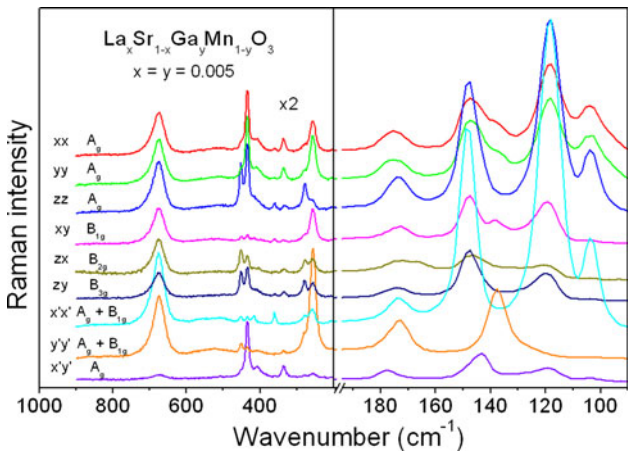

Fig. 1 Polarized Raman spectra of $La_{1-x}Sr_xGa_{1-y}Mn_yO_3$ with $x = y = 0.005$ (sample A) recorded in different scattering configurations

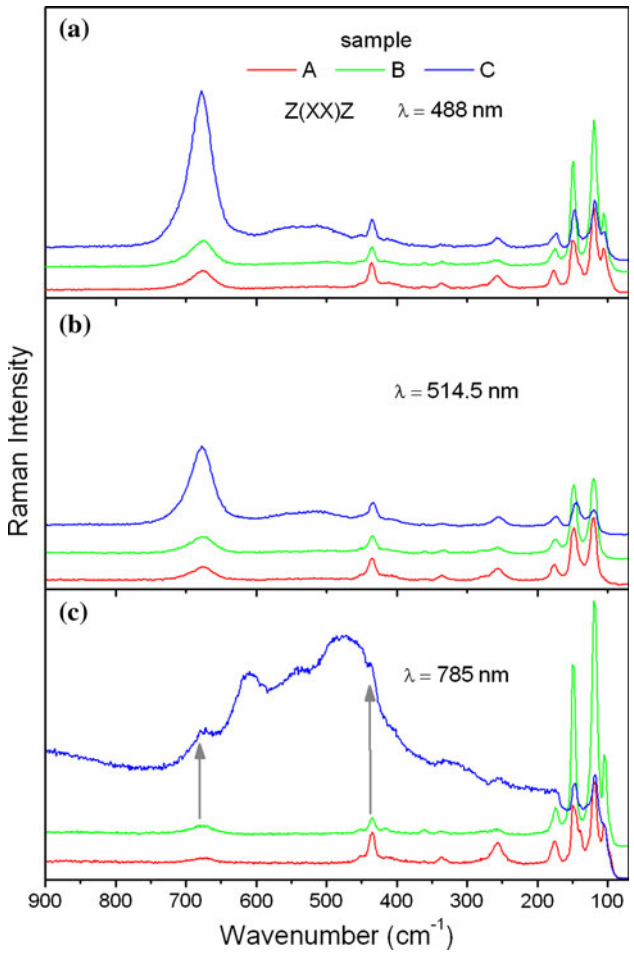

Fig. 2 Polarized Raman spectra of samples A, B and C recorded in Z(XX)Z scattering configuration with excitation wavelength: **a** 488 nm, **b** 514.5 nm and **c** 785 nm

spectrum of the OR $LaMnO_3$ compound shows two intensive spectral features at 480 and 610 cm^{-1} and one weak band at 280 cm^{-1}, while the spectrum of the paramagnetic $CaMnO_3$ compound of the same OR *Pbnm* space group is much different. Firstly, it does not contain spectral features above 500 cm^{-1} (stretching modes) and secondly, in this spectrum, two doublets around 240 and 460 cm^{-1} appear assigned to tilt and bending vibrations, respectively. Additionally, two modes are observed below 200 cm^{-1}. Sacchetti et al. [18] have reported infrared and Raman investigations of $SrMnO_3$ manganite. Because the tolerance factor of $SrMnO_3$ (SMO) is very close to unity ($t = 1.05$), it can be synthesized in both cubic and hexagonal structure depending on the growing procedure. The RT Raman spectrum of the hexagonal SMO compound is dominated by three strong features at 344, 440 and 644 cm^{-1} and two weak bands at 243 and 551 cm^{-1}. Two low-frequency modes at 243 and 344 cm^{-1} are related to displacements of Mn ions, while the high-frequency modes at 440, 551 and 644 cm^{-1} are related to tilt/bending, asymmetric and symmetric stretching vibrations of MnO_6 octahedra, respectively.

Recently, Baldini et al. [19] have presented Raman investigation of $LaMn_{1-x}Ga_xO_3$ compounds with x varying in the range 0–0.8 and high-pressure measurements for samples with $x = 0.2$ and 0.6. Although the lowest content of Mn in the $LaMn_{1-x}Ga_xO_3$ sample studied by Baldini et al. is 0.2 ($x = 0.8$), which is significantly higher in comparison with our samples, the structure of the Raman modes above 480 cm^{-1} is quite similar. Thus, we propose the following mode assignment in this spectral range for $La_{1-x}Sr_xGa_{1-y}Mn_yO_3$ crystals: the spectral features at around 510 and 560 cm^{-1} are assigned to the bending and JT-active antisymmetric stretching (AS) vibrational modes of MnO_6 octahedra, respectively, the mode located at about 675 cm^{-1} is attributed to symmetric stretching (SS) vibrational modes of MnO_6 octahedra. The Raman modes below 200 cm^{-1} can be assigned to vibrations of A-site cations. As seen from Fig. 1, taking into consideration all scattering configurations, eight Raman modes are observed in the range 100–200 cm^{-1}. In this spectral range, the number of Raman modes detected for samples A, B and C is comparable. However, slight differences in the positions of these modes for the samples studied are observed and could be explained by slight changes in the average atomic mass of A-site cation. With increasing Sr content, the average atomic mass of A-site cation decreases. Taking this into account, it is expected that the frequency of A-site cation vibrations should slightly increase. Low-wavenumber spectra do not confirm this expectation. Hence, the valency of doping ions should be considered as well. The mixed valency of A-site cations in crystal is caused by substitution of La^{3+} ions by Sr^{2+} ions. With increasing Sr^{2+} content, the average valency of the cations at the A-site decreases. The change in wavenumber of translational motions of A-site cations can be caused mainly by two factors: change in average atomic mass and mixed valency of A-site cation. Thus, a slight decrease in the wavenumber of the lattice modes involving A-site cation motions can be successfully explained by a superposition of these two competing effects. In the range 200–300 cm^{-1}, two modes at 256 and 278 cm^{-1} are observed. The first mode can be assigned to GaO_6 tilt, while the second one to mixed vibrations of A-site and apical O(1) atoms in the *xy* plane. It is worth noting that different combinations of displacements of the oxygen atoms in octahedra (in-plane O(2) and apical O(1) atoms) give rise to four tilt modes ($A_g + B_{1g}$) and ($B_{2g} + B_{3g}$) and two bending modes ($A_g + B_{1g}$) [12]. As confirmed in papers [12, 14, 20], the modes of B_{2g} and B_{3g} symmetry have very low intensity. Moreover, the Raman modes grouped in brackets have very similar wavenumbers because they correspond to the same atomic movements around the *x* or *y* axis. The tilt and bending modes with A_g symmetry correspond to rotations around the *y* axis, while B_{1g} modes correspond to the same atomic movements but around the *x* axis, therefore A_g and B_{1g} modes are expected to be very similar in frequency. Moreover, the displacement of O(1) atoms in these modes is, in fact, a stretching of R–O(1) bonds. Martin-Carron et al. [12] claim that the stretching mode frequencies correlate to Mn–O bond distances, while the R–O bond and octahedra tilt angle dominate the bending and tilt modes, respectively. Two very low-intense modes are observed in the range 320–370 cm^{-1} (see Fig. 1) and they can be assigned to the remaining two tilts ($B_{2g} + B_{3g}$). These modes are detected for samples A and B, while they are practically not observed for sample C (Fig. 2a). Taking into account all scattering configurations (see Fig. 1), four bands of different intensity are observed in the 400–460 cm^{-1} spectral range. These modes are assigned to out-of-phase bending vibrations and to out-of-phase O2 scissors [14].

Figure 2a, b, c shows the polarized Raman spectra recorded in the XX scattering configuration for samples A, B and C using 488, 514.5 and 785 nm laser lines, respectively. The scale of the vertical axis of each of three parts a, b and c of this figure has the same maximum value. The Raman spectra obtained for samples A and B are practically qualitatively independent of the excitation photon energy (laser line wavelength). However, an essential qualitative difference in the Raman spectrum of sample C is observed if 785 nm wavelength of laser light is used. For a near infrared excitation, a strong increase in the background and a change in the structure of the Raman spectrum are observed. These changes cannot be ascribed to thermal effects related to local overheating of the sample

(small laser power density was applied) or photodegradation of the sample but can be rather related to different resonant conditions (resonance effects connected with d–d transitions in Mn ions). Major changes in the spectrum appear above 350 cm^{-1} where strong, broad and overlapped bands with maxima at about 470, 540, 610 and 675 cm^{-1} appear. The Raman modes at 172, 255 and 433 cm^{-1} recorded in the XX scattering configuration using 488 and 514.5 nm excitation laser lines are not observed if the spectrum is recorded with a near infrared excitation (785 nm). These modes are overlapped by the mentioned new bands. Moreover, the modes at 116, 145 and 675 cm^{-1} are recorded in the Raman spectra obtained using both visible and near infrared excitation laser lines. The strongest mode centred at 675 cm^{-1} in the spectrum recorded using 488 nm excitation has a rather weak intensity in the spectrum recorded using 785 nm excitation line. Figure 3 shows the spectra of sample C taken using different excitation wavelengths but after normalization. The spectra are vertically shifted for better visualization. Normalization process takes into account the reflectance, the λ^4 scaling factor and detector efficiency in different spectral ranges. Through this process, a correct determination of intensity and integral intensity of the mode required is possible. The modes recorded below 160 cm^{-1} have the highest intensity for 785 nm excitation and lowest for 514.5 nm excitation, while the mode at about 675 cm^{-1} has a higher intensity for 488 nm excitation. As seen from Fig. 3, the difference in the intensity of this mode for 514.5 and 785 nm excitations is rather small. It was confirmed by the fit of the spectra with Lorentzian shape lines that indicated comparable intensity of 675 cm^{-1} mode for both excitation lines.

Temperature measurements of Raman spectra for samples A, B and C were performed with a step of 0.1 K in temperature ranges suitable for each sample in two scattering configurations XX and XY. The heating rate was 0.1 K/min, and temperature was stabilized by 5 min before each measurement. Figure 4 shows the temperature evolution of selected Raman spectra recorded for sample A in XY scattering configuration in the range 406.7–407.7 K, which includes the temperature of the OR–RH phase transition. As seen from this figure, the number of Raman modes appearing in the spectra significantly decreases after the phase transition. This is in full consistence with the group theory calculations that predict a reduction in the number of Raman-active modes from 24 ($7A_g + 7B_{1g} + 5B_{2g} + 5B_{3g}$) for the OR phase to 5 ($A_{1g} + 4E_g$) for the RH phase. The Raman spectra taken before and after the phase transition for samples A, B and C in XY scattering configuration are presented in Fig. 5a–c. In the Raman spectrum of high-temperature phase (RH structure) obtained for sample A (see Fig. 5a), three distinct modes are observed in the 100–900 cm^{-1} spectral range. These modes are recorded at about 165, 447 and 680 cm^{-1}, while the fourth mode at 257 cm^{-1} has a significantly larger intensity in XX scattering configuration. For sample B (Fig. 5b), four modes at comparable wavenumbers are observed. For sample C, two stronger modes at 165 and 680 cm^{-1} and two of lower intensity at 447 and around 550 cm^{-1} are observed (Fig. 5c). The E_g modes are observed at 165 and 447 cm^{-1}, while A_{1g} mode at 257 cm^{-1}. The modes at 165 and 447 cm^{-1} are attributed to A ion vibration and BO_6 bending/A–O stretching vibration, respectively, while the mode at 257 cm^{-1} is assigned to the oxygen octahedron tilt. An additional E_g mode assigned to the antistretching vibration is expected in

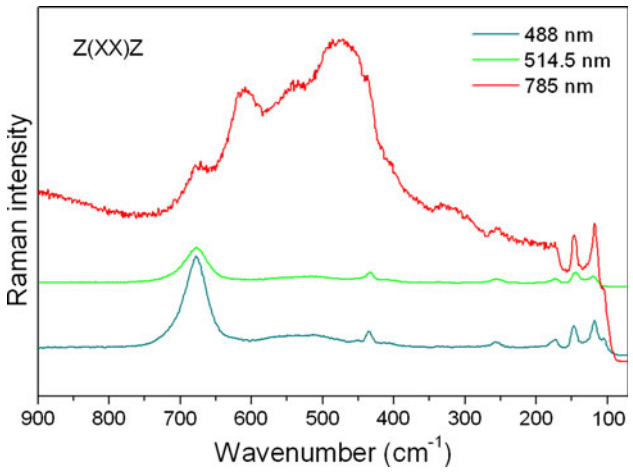

Fig. 3 Normalized Raman spectra of sample C recorded in Z(XX)Z scattering configuration with excitation wavelength: **a** 488 nm, **b** 514.5 nm and **c** 785 nm

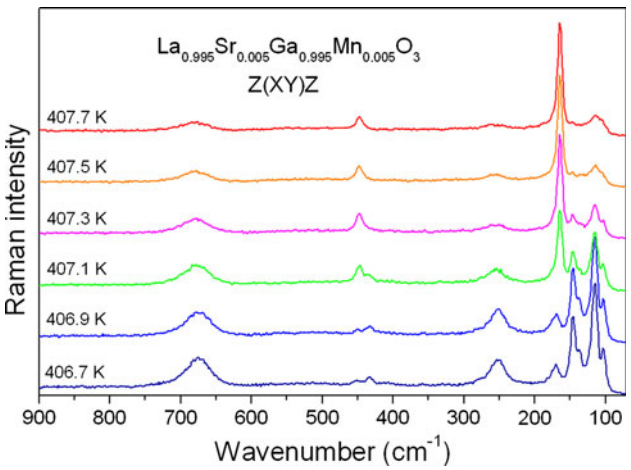

Fig. 4 Temperature evolution of selected Raman spectra recorded for sample A in Z(XY)Z scattering configuration

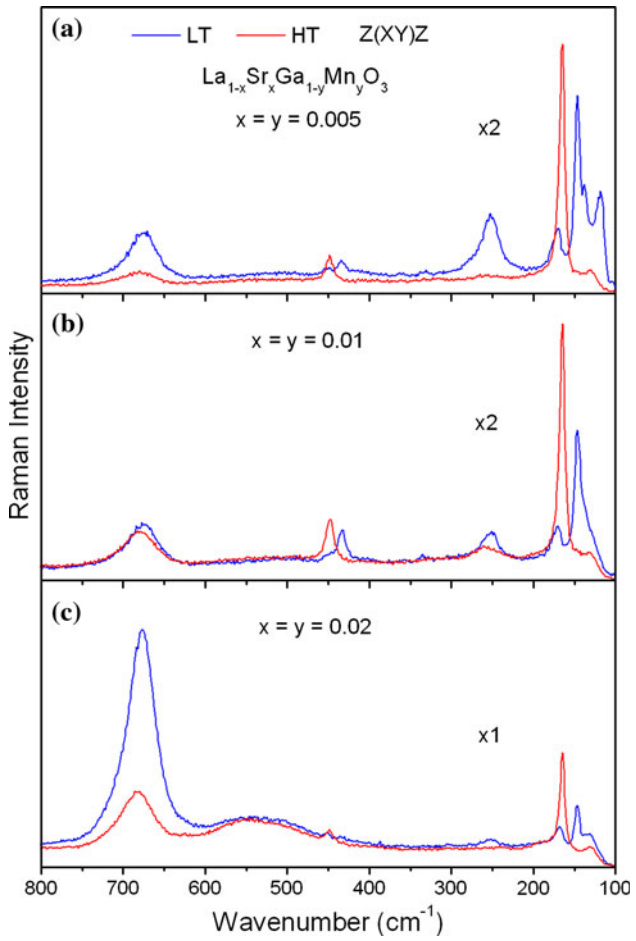

Fig. 5 Raman spectra recorded below and above phase transition temperature in Z(XY)Z scattering geometry with 488 nm excitation wavelength: **a** sample A, **b** sample B and **c** sample C

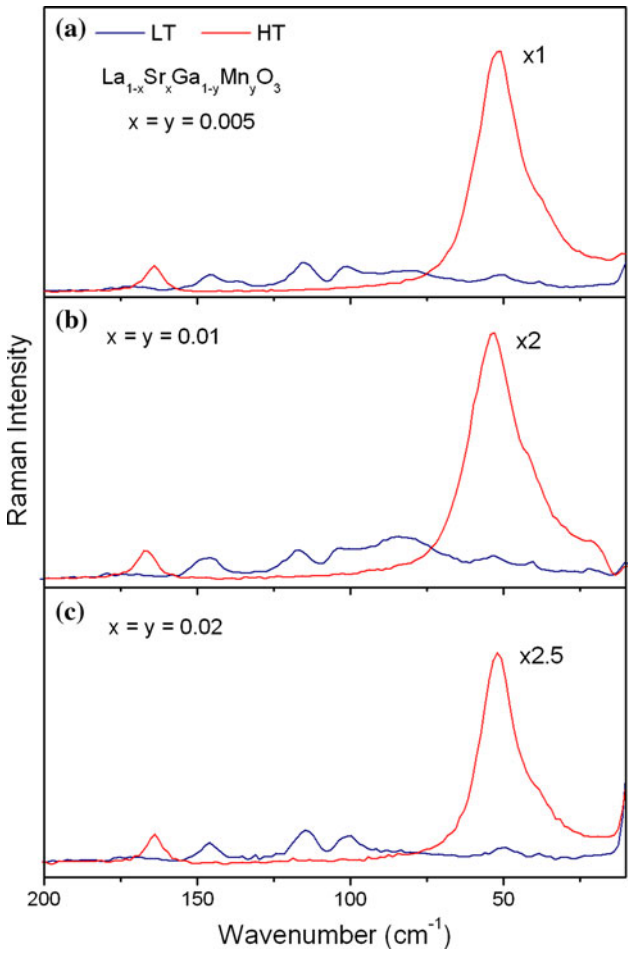

Fig. 6 Non-polarized Raman spectra recorded below and above phase transition temperature using NExT filter with 488 nm excitation wavelength: **a** sample A, **b** sample B and **c** sample C

the range 550–600 cm^{-1}. Broad and rather two-component band at around 550 cm^{-1} is detected only for sample C. In our earlier study of $La_{1-x}Sr_xGa_{1-y}Mn_yO_3$ crystal with a higher Sr and Mn contents ($x = 0.05$; $y = 0.06$) [3], a band at about 560 cm^{-1} was noted that could be assigned to the antistretching vibration of MnO_6 octahedra [12, 19]. The mode recorded at 680 cm^{-1} similarly as that observed in the spectrum of the low-temperature *Pbnm* structure can be assigned to the symmetric stretching vibration of MnO_6 octahedra. The symmetric stretching vibration of A_{2g} symmetry is not allowed in the high-temperature phase with $R\bar{3}c$ space group. However, this mode is observed in the spectra of all samples investigated in the high-temperature phase and its activity is related to distortion of MnO_6 octahedra. The wavenumber value of this mode increases at the phase transition by about 4 cm^{-1}. It means that after the phase transition, a rearrangement of the crystal lattice to RH phase causes a small reduction in the bond length of MnO_6 octahedra. The last E_g mode is expected in the low-wavenumber range. Thus, complementary temperature measurements were performed using a special filter—Renishaw NExT filter—which allows us to record the Raman spectra below the edge filter cut-off. The configuration of our μ-Raman system does not allow measurement of polarized Raman spectra if a NExT filter is applied. The non-polarized low-wavenumber Raman spectra recorded with the NExT filter before and after the phase transition for samples A, B and C are presented in Fig. 6a–c. As follows from this figure, the expected E_g mode is observed at about 52 cm^{-1}. The intensity of this mode decreases with increasing Sr and Mn contents. Moreover, it is worth noting that the intensity of this mode is several times higher than that of the mode at 165 cm^{-1}, which was the strongest in the spectrum recorded with the edge filter (Fig. 5a, b). However, we cannot directly compare the spectra from Figs. 5 and 6, because the optical efficiency of the system working with the NExT filter is more than ten times lower in comparison with that

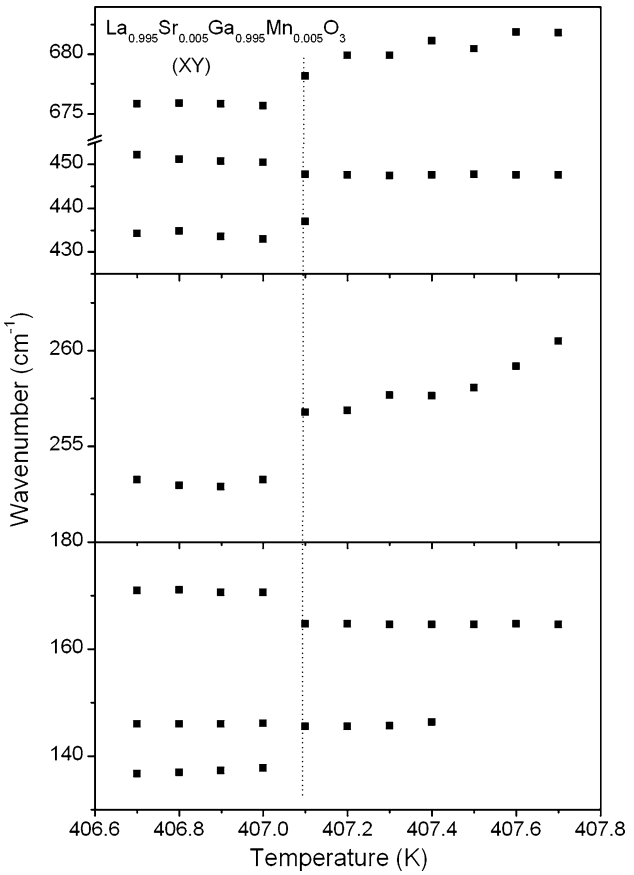

Fig. 7 Temperature variation of Raman mode positions of sample A

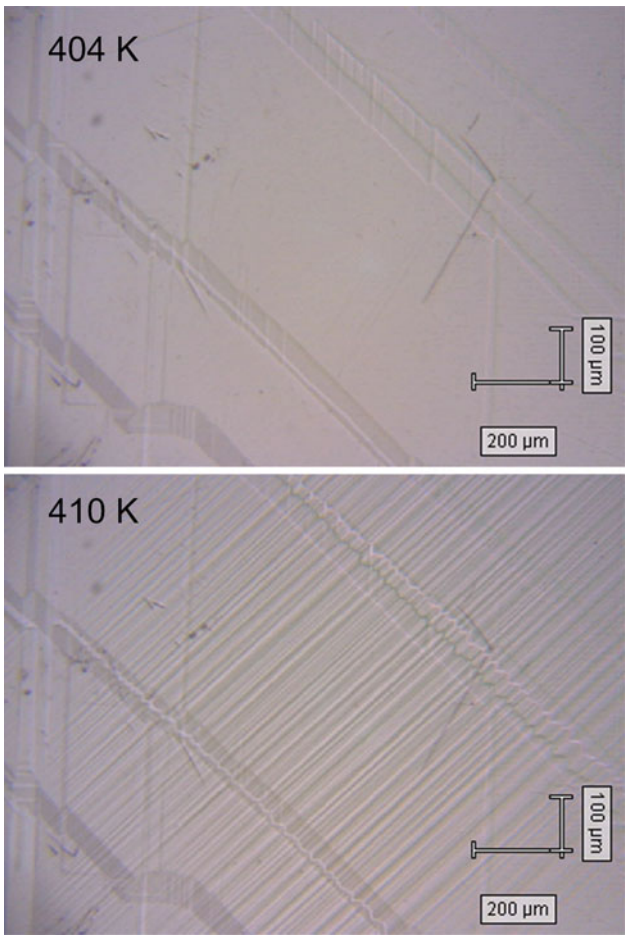

Fig. 8 Optical images of sample A before (404 K) and after (410 K) phase transition obtained using ×5 objective

employing the edge filter. Temperature changes of the Raman modes positions, except that of the low-wavenumber tilt mode at 52 cm^{-1} for sample A in XY scattering configuration, are presented in Fig. 7. Such dependencies for samples B and C have also been drawn but are not presented here.

The temperature-induced phase transitions from the OR *Pbnm* to the RH $R\bar{3}c$ phase in samples A, B and C are observed at 407.1, 398.1 and 379.9 K, respectively. The shift of the phase transition temperature is caused by a change in the ionic radius of the atoms that occupies A-site, as the ionic radii of La^{3+} and Sr^{2+} are much different. There is a small difference in ionic radius of the B-site cations substituents (manganium and gallium atoms). On average, the temperature decrease with increasing Sr and Mn contents is equal to about 20 K/at%.

Optical images of the surface of sample A obtained using ×5 microscope objective before (404 K) and after (410 K) phase transition are presented in Fig. 8. Observed plane of the crystal $(001)_{OR}$ is not optically homogeneous and microstructure (twin-related domains) is clearly seen. Raman mapping was applied to detect domain structure using ×50 LWD objective. Point Raman mapping involves acquiring Raman spectra sequentially from series of positions on the crystal surface, and then analysing the spectra to produce images indicating the variation of key spectral parameters. The Raman maps of dimensions 48 × 24 μm^2 from selected area on the sample surface after phase transition to high-temperature $R\bar{3}c$ RH phase was recorded. The measurements were carried out at 385, 400 and 410 K for samples C, B and A, respectively. Raman map consists of 561 points and was created from the intensity at the maximum of the lattice mode located at 164 cm^{-1}. The Raman maps obtained for samples A, B and C are presented in Fig. 9.

To evaluate the high-temperature phase stability, the Raman spectra of samples A, B and C were measured at higher temperatures in XX scattering configuration. In Fig. 10a–c, we present the spectra collected for each sample at 300, 450 and 800 K, after the Bose–Einstein correction. It is known that at 300 K, all samples have the OR structure, while at 450 K the RH one. Comparing the Raman spectra of RH phase recorded at 450 and 800 K for

Fig. 9 The Raman maps of dimensions 48 × 24 µm^2 from selected area of samples A, B and C obtained at 410, 400 and 385 K, respectively

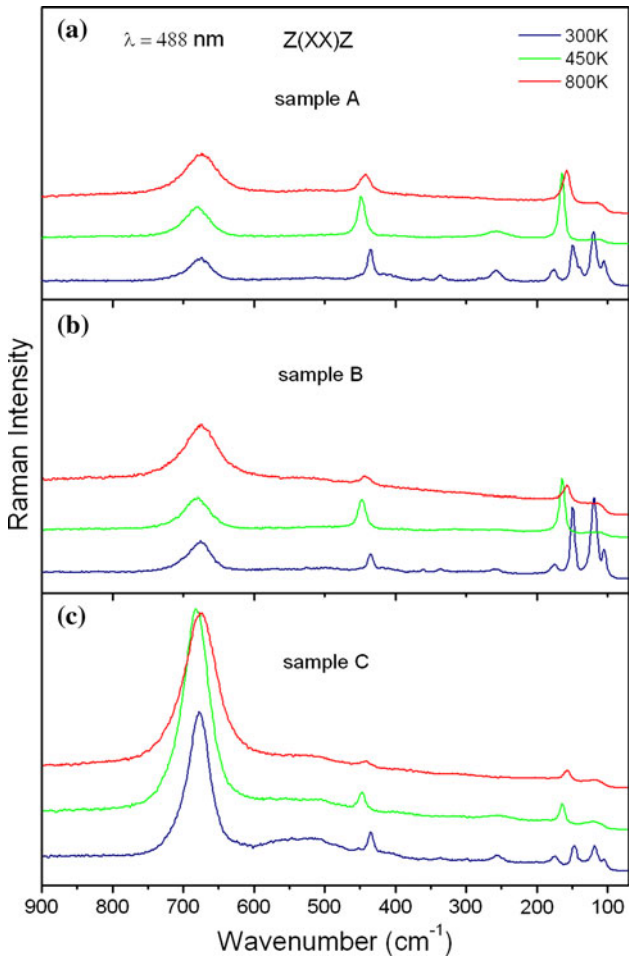

Fig. 10 Raman spectra recorded at 300, 450 and 800 K in Z(XX)Z scattering configuration with 488 nm excitation wavelength: **a** sample A, **b** sample B and **c** sample C

each sample separately, it is obvious that the structure of bands in these spectra is very similar at these two temperatures except A_{1g} mode at about 250 cm^{-1}, which vanishes in all samples at 800 K. Because this mode is assigned to tilt vibrations of BO_6 octahedra, its disappearance has to be related to a significant decrease in the tilt angle or even disappearance of octahedral tilts. Additionally, the increase in the width and red-shift of the bands with temperature is observed. The broadening of bands is normal anharmonic behaviour when temperature increases, while the red-shift can be explained by thermal expansion of crystal lattice. It is worth noting that even at 800 K in the spectra of all samples, the peaks are quite sharp such a high temperature. However, the intensity of peaks recorded at 156 and 442 cm^{-1} depends on Sr and Mn contents and takes the lowest value for sample C.

Martin-Carron et al. [12] reported the Raman spectrum of $LaMnO_3$ with a cooperative Jahn–Teller distortion. Its Raman spectrum was dominated by stretching vibrations. The authors presented the spectra recorded at RT and above 800 K. The intensity of the Raman modes above 800 K decreased drastically when compared to that in the RT spectrum. However, some spectral features were noted in the high-frequency range and interpreted as corresponding to stretching modes, while the tilt and bending modes almost vanished. The authors concluded that dynamic distortions of the MnO_6 octahedra cannot give rise to the quite narrow peaks assigned to tilt and bending vibrations, but are manifested as the broad stretching bands. Because the Raman spectra of samples A, B and C show spectral features in the range of stretching, bending and A-site cation vibrations even at 800 K (Fig. 10a–c), in

these compounds cooperative JT distortion is present and the crystal structure is stable up to 800 K.

Conclusions

Single crystals of $La_{1-x}Sr_xGa_{1-y}Mn_yO_3$ with $x = y = 0.005$ (sample A), 0.01 (sample B) and 0.02 (sample C) have been studied by Raman spectroscopy. Complete assignment of Raman modes has been carried out analysing a set of polarized spectra recorded for a single crystal with $x = y = 0.005$. The increase in the Mn content causes significant changes in the Raman spectra, especially in the high-wavenumber spectral range. The Raman spectrum of $La_{1-x}Sr_xGa_{1-y}Mn_yO_3$ compound with $x = y = 0.02$ is mainly dominated by MnO_6 internal vibrations. Moreover, a change in the spectrum of this crystal is observed when the 785-nm excitation line is used. Temperature measurements were performed for all samples. The Raman spectroscopy provides evidence for OR–RH phase transition. Significant reduction in the number of Raman modes at the phase transition is experimentally observed, in good agreement with the group theory predictions. The temperature-induced phase transitions from OR *Pbnm* to RH $R\bar{3}c$ phase of samples A, B and C are observed at 407.1, 398.1 and 379.9 K, respectively. The temperature of the phase transition decreases with increasing Sr and Mn contents at the rate close to 20 K/at% of dopants. Optical images and Raman maps recorded for all samples investigated confirm the existence of microstructure in RH phase.

Acknowledgements This work was supported by Research Project of Poznan University of Technology No. 511/64-001/11 DS-PP.

References

1. Suda J, Mori T, Saito H, Kamishima O, Hattori T, Sato T (2002) Phys Rev B 66:174302
2. Pathak S, Kalidindi SR, Moser B, Klemenz Ch, Orlovskaya N (2008) J Eur Ceram Soc 28:2039
3. Glowacki M, Runka T, Domukhovski V, Diduszko R, Mirkowska M, Berkowski M, Dabrowski B (2011) J Alloys Compd 509:1756
4. Wei T, Ji Y, Meng X, Zhang Y (2008) Electrochem Commun 10:1369
5. Inagaki T, Miura K, Yoshida H, Fujita J, Nishimura M (1999) Solid State Ionics 118:265
6. Ishihara T, Matsuda H, Takita Y (1994) J Am Chem Soc 116:3801
7. Ishihara T, Matsuda H, Takita Y (1995) Solid State Ionics 79:147
8. Yashima M, Nomura K, Kageyama H, Miyazaki Y, Chitose N, Adach K (2003) Chem Phys Lett 380:391
9. Yao W, Tang Z, Zhang Z, Luo S, Li J, Tan Q (2003) Mater Sci Eng B 99:309
10. Fu Q, Xu X, Peng D, Liu X, Meng G (2003) J Mater Sci 38:2901. doi:10.1023/A:1024496805673
11. Sanjuan ML, Orera VM, Merino RI, Blasco J (1998) J Phys Condens Matter 10:11687
12. Martin-Carron L, De Andres A, Martinez-Lopez MJ, Casais MT, Alonso JA (2002) Phys Rev B 66:174303
13. Martin-Carron L, De Andres A (2001) Eur Phys J B 22:11
14. Iliev MN, Litvinchuk AP, Hadjiev VG, Wang Y-Q, Cmaidalka J, Meng E-L, Sun Y–Y, Kolev N, Abrashev MV (2006) Phys Rev B 74:214301
15. Abrashev MV, Bäckström J, Börjesson L, Popov VN, Chakalov RA, Kolev N, Meng R-L, Iliev MN (2002) Phys Rev B 65: 184301
16. Granado E, Sanjurjo JA, Rettori C, Neumeier JJ, Oseroff SB (2000) Phys Rev B 62:11304
17. Liarokapis E, Leventouri Th, Lampakis D, Palles D, Neumeier JJ, Goodwin DH (1999) Phys Rev B 60:12758
18. Sacchetti A, Baldini M, Crispoldi F, Postorino P, Dore P, Nucara A, Martin C, Maignan A (2005) Phys Rev B 72:172407
19. Baldini M, Di Castro D, Cestelli-Guidi M, Garcia J, Postorino P (2009) Phys Rev B 80:045123
20. Iliev MN, Abrashev MV, Lee H-G, Popov VN, Sun YY, Thomsen C, Meng RL, Chu CW (1998) Phys Rev B 57:2872